

Machine Learning Changes the Rules for Flux Limiters

Nga Nguyen-Fotiadis,¹ Michael McKerns,¹ and Andrew Sornborger¹
Information Sciences, CCS-3, Los Alamos National Laboratory, Los Alamos, NM 87545, USA

(*Electronic mail: sornborg@lanl.gov)

Learning to integrate non-linear equations from highly resolved direct numerical simulations (DNSs) has seen recent interest for reducing the computational load for fluid simulations. Here, we focus on determining a flux-limiter for shock capturing methods. Focusing on flux limiters provides a specific plug-and-play component for existing numerical methods. Since their introduction, an array of flux limiters has been designed. Using the coarse-grained Burgers' equation, we show that flux-limiters may be rank-ordered in terms of their log-error relative to high-resolution data. We then develop theory to find an optimal flux-limiter and present flux-limiters that outperform others tested for integrating Burgers' equation on lattices with $2\times$, $3\times$, $4\times$, and $8\times$ coarse-grainings. We train a continuous piecewise linear limiter by minimizing the mean-squared misfit to 6-grid point segments of high-resolution data, averaged over all segments. While flux limiters are generally designed to have an output of $\phi(r) = 1$ at a flux ratio of $r = 1$, our limiters are not bound by this rule, and yet produce a smaller error than standard limiters. We find that our machine learned limiters have distinctive features that may provide new rules-of-thumb for the development of improved limiters. Additionally, we use our theory to learn flux-limiters that outperform standard limiters across a range of values (as opposed to at a specific fixed value) of coarse-graining, number of discretized bins, and diffusion parameter. This demonstrates the ability to produce flux limiters that should be more broadly useful than standard limiters for general applications.

I. INTRODUCTION

Numerically integrating fluid equations on a coarse grid relative to a fully resolved integration of a given problem (coarse-graining) is of both historical and current interest¹⁻⁵ since it can significantly reduce the computational time required for a given simulation. With the advent of modern machine learning methods, a number of attempts have been made to develop improved coarse-grained models⁶, including for 3D Eulerian⁷ and Navier-Stokes turbulence⁸, buoyancy-driven, variable density turbulence⁹, and molecular-level simulations¹⁰.

In this paper, our focus will be machine learning an accurate local integrator for the coarse-grained, 1-D viscous Burgers' equation¹¹. Burgers' equation is the simplest fluid equation admitting shocks^{12,13} and is exactly integrable. Numerically integrating shocks is complicated by the Gibbs effect¹⁴, where, when a discontinuity develops, unstable oscillations develop in a numerical simulation. This behavior may be corrected using shock capturing methods¹⁵⁻¹⁹. Shock capturing methods rely on *flux limiters* - non-linear interpolations between high- and low-resolution integration schemes used in a numerical simulation to keep a shock solution monotonic, thereby eliminating spurious oscillations.

Harten¹⁸ provided a framework for constructing non-linear, monotonicity preserving flux limiters. At present, a large number of flux limiters have been defined and used in the literature²⁰. Different forms of flux limiter have been shown to have differing accuracy and convergence performance²⁰. And criteria have been studied for determining what parameter regions are appropriate for different classes of limiter²¹.

Since Burgers' equation is exactly integrable, it is straightforward to generate accurate, high-resolution data from which flux limiters may be tested using a machine learning approach. This setting also provides a good testing ground for developing methodology and evaluating which flux limiters are the

best (for one particular equation, or potentially for multiple shock-forming equations), and for comparing existing flux limiters with those learned from data.

Below, we will introduce the Cole-Hopf solution to the inviscid Burgers' equation, show how to use it to test DNS training data, and define our flux limiters. We will then present a cost function allowing us to compare predicted outcomes from a discretized flux limiter with high-resolution DNS training data. Next, we will optimize the cost function for a given set of data resulting in a regression analysis solvable with standard linear algebraic methods. We then apply this analysis to a training dataset to learn optimal flux limiters from coarse-grained data. We compare these optimized, coarse-grained flux limiters with a large set of other flux limiters and show that they outperform them over the set of coarse-grainings. We finally incorporate our regression analysis within a larger, hyper-parameter optimization framework to find an optimal discretization of the flux limiter over a range of parameters, including coarse-graining, number of discretization bins, and diffusion parameter.

II. BACKGROUND

A. Exact Solution of Inviscid Burgers' Equations

The viscous Burgers' equation¹¹ written in conservative form is

$$\frac{\partial u}{\partial t} + \frac{\partial}{\partial x} \left(\frac{u^2}{2} - \nu \frac{\partial u}{\partial x} \right) = 0. \quad (1)$$

It may be solved exactly with the Cole-Hopf transform¹³,

$$u = -2\nu \frac{1}{\phi} \frac{\partial \phi}{\partial x}. \quad (2)$$

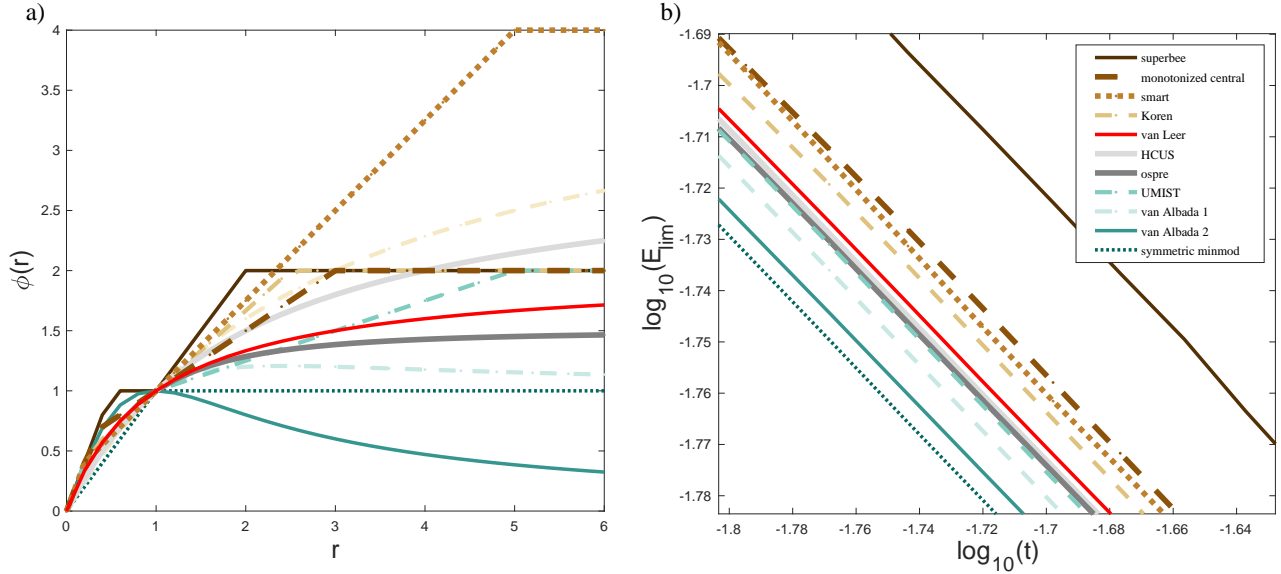


FIG. 1. A set of flux limiters and their log-error relative to high resolution data. In this figure and in Fig. 2, we use the same colors and patterns to indicate a particular flux limiter. For instance, the van Leer limiter is plotted in solid red. The legend for both panel a) and panel b) is shown in panel b). a): 11 flux limiters, $\phi_i(r)$, where i ranges over a set of standard flux limiters (see legend in b)), plotted as a function of flux ratio r . All flux limiters, by design²¹, go through the point, $(r, \phi) = (1, 1)$. b): Log-error computed for each standard limiter in a) with error, $E_{\text{lim}} = e_i - e_{\text{hres}}$, with e_i the shock capturing solution with limiter, i , and e_{hres} the $2\times$ coarse-grained high-resolution solution. Here, we compare against the standard sinusoidal solution of Burgers' equation. Note that while most limiters are bowed out below $r < 1$, the better performing (lower error, in green) limiters tend to be comparatively (with regard to van Leer, in red) bent down for $r > 1$.

For periodic boundary conditions (those considered here), the transform results in a diffusion equation

$$\frac{\partial \phi}{\partial t} = \nu \frac{\partial^2 \phi}{\partial x^2}, \quad (3)$$

which may be solved with Fourier methods. Finally, the Cole-Hopf transform is inverted to recover the solution in the original coordinates.

We used a discretized version of the Cole-Hopf transform on a finely resolved lattice to generate simulation data. This approach works well for moderately sized lattices, but has instabilities for larger lattices when ν becomes small²². Thus, for our flux limiter optimization procedure, below, we used a first-order, but very accurate scheme to generate our training and test data and validated the scheme, which is stable for any sized lattice, on simulations on smaller lattices by comparing with the discretized Cole-Hopf transform (See Appendix A). We call data generated in this way *exact* or *high-resolution* data. Note that this solution method can resolve shocks without the need for flux limiters and thus provides good data to test flux limiters in shock capturing integration schemes. For equations with no analytical solution, high-resolution data from finely resolved DNSs would need to be used.

B. Flux Limiters

We use a semi-discrete scheme to integrate initial conditions from coarse-grained data selected at different resolutions

from previously generated exact data. The integration scheme takes the general form

$$\frac{du_i}{dt} + \frac{1}{\Delta x_i} [G(u_{i+\frac{1}{2}}) - G(u_{i-\frac{1}{2}})] = 0. \quad (4)$$

Here, i is a cell index, and $G(u_{i-\frac{1}{2}})$ and $G(u_{i+\frac{1}{2}})$ denote edge fluxes. The edge fluxes are non-linear interpolations between high- and low-resolution fluxes

$$G(u_{i+\frac{1}{2}}) = (1 - \phi(r_i)) f_{i+\frac{1}{2}}^{\text{low}} + \phi(r_i) f_{i+\frac{1}{2}}^{\text{high}}, \quad (5)$$

$$G(u_{i-\frac{1}{2}}) = (1 - \phi(r_{i-1})) f_{i-\frac{1}{2}}^{\text{low}} + \phi(r_{i-1}) f_{i-\frac{1}{2}}^{\text{high}}. \quad (6)$$

Here, f^{low} indicates a low-resolution flux, typically first-order, which does not suffer from Gibbs phenomena, and f^{high} indicates a high-resolution flux to integrate smoother regions of a solution. The flux limiter, $\phi(r)$, is a function of the flux ratio,

$$r_i = \frac{u_i - u_{i-1}}{u_{i+1} - u_i}. \quad (7)$$

A large number of flux limiters have been proposed and used. For instance, the van Leer flux limiter²³ takes the form

$$\phi(r) = \frac{r + |r|}{1 + |r|}. \quad (8)$$

Note that this flux limiter and all of the flux limiters that we consider (see Fig. 1 and Tab. VII) here are (piecewise) continuous and zero for $r \leq 0$.

III. METHODS

A. A Shock Capturing Integration Method for Burgers' Equation

For low- and high-resolution, we chose Lax–Friedrichs (LF)

$$f_{i\pm\frac{1}{2}}^{\text{low}} = f_{i\pm\frac{1}{2}}^{\text{LF}} = \frac{1}{2}[F(u_i) + F(u_{i+1}) \mp \alpha \frac{\Delta x}{\Delta t}(u_{i\pm 1} - u_i)];$$

$$\alpha = \max_u \left| \frac{\partial F}{\partial u} \right| \quad (9)$$

and Lax-Wendroff (LW) fluxes

$$f_{i\pm\frac{1}{2}}^{\text{high}} = f_{i\pm\frac{1}{2}}^{\text{LW}} = \frac{1}{2}[F(u_i) + F(u_{i+1}) \mp \frac{\Delta t}{\Delta x} \left(\frac{\partial F}{\partial u}(u_{i\pm\frac{1}{2}}) \right) (F(u_{i\pm 1}) - F(u_i))], \quad (10)$$

where $F = \frac{u^2}{2} - v \frac{\partial u}{\partial x}$ is the flux from Burgers' equation. Eq. (4) now becomes:

$$u_i(t_{n+1}) = u_i(t_n) - \frac{\Delta t}{\Delta x} \Delta F^i \quad (11)$$

with

$$\Delta F^i = \Delta F_1^i + \phi(r_i) \Delta F_2^i + \phi(r_{i-1}) \Delta F_3^i, \quad (12)$$

where ΔF_1^i , ΔF_2^i , and ΔF_3^i can be written explicitly as:

$$\begin{aligned} \Delta F_1^i &= f_{i+\frac{1}{2}}^{\text{LF}} - f_{i-\frac{1}{2}}^{\text{LF}}, \\ \Delta F_2^i &= f_{i+\frac{1}{2}}^{\text{LW}} - f_{i+\frac{1}{2}}^{\text{LF}}, \\ \Delta F_3^i &= -(f_{i-\frac{1}{2}}^{\text{LW}} - f_{i-\frac{1}{2}}^{\text{LF}}). \end{aligned} \quad (13)$$

In Fig. 1(a), we plot a set of 12 different flux-limiters from the literature. An important feature to note in these flux limiters is that they all pass through the point $\phi(1) = 1$. This is due to a requirement of second-order accuracy of the shock capturing scheme and Lipschitz continuity of $\phi(r)$ ²¹. In Fig. 1(b), we show the difference between solutions computed with the various flux limiters and high-resolution data. In this example, both simulation and high-resolution data are coarse grained at $2\times$ (i.e. initial conditions for each simulation were subsampled at every other grid point from high-resolution data, integrated with a shock-capturing scheme for time t , then compared to subsampled high-resolution data at time t). In (Fig. 1(b)), we see an ordering where some flux limiters perform better than others for predicting coarse-grained data. Note that, although we plot the errors over a short time, the errors retain the same ordering over the whole integration. Thus, we can define an ordering of the limiters.

At this point, the question as to what the optimal flux limiter is arises. In this study, we set up the problem of how to find a flux limiter, $\phi(r)$, that is optimal with respect to certain criteria. We will train a piecewise linear flux limiter using an exact dataset (Appendix A) and compare it with the 11 flux limiters shown in Fig. 1(a).

B. Flux Limiter Discretization

We discretize the flux-limiter that we will optimize with machine learning methods, $\phi(r)$, in piecewise linear segments, where the k 'th segment has the form,

$$\begin{aligned} \phi_k(r) &= \phi_0 + b_1(r_2 - r_1) + b_2(r_3 - r_2) + \dots + b_k(r - r_k) \\ &\quad + 0_{k+1} + \dots + 0_K, \end{aligned} \quad (14)$$

and $r \in [r_k, r_{k+1}]$, $k \in \{1, \dots, K\}$, $\phi_0 = 0$, and b_i are slope coefficients. Note that for $r \leq 0$, $\phi(r) = 0$ and for $r = r_K$, all terms in Eq. (14) are non-zero. Below, we use vector notation, $\mathbf{b} = [b_1, b_2, \dots, b_k, b_{k+1}, \dots, b_K]^T$ for slope coefficients. Eq. (14) can be rewritten as $\phi_k(r) = \mathbf{b}^T \Delta \mathbf{r}_k$ with $\Delta \mathbf{r}_k$ defined as

$$\Delta \mathbf{r}_k = [r_2 - r_1, r_3 - r_2, \dots, r - r_k, 0, \dots, 0]^T. \quad (15)$$

C. Learning an Optimal Discretized Flux Limiter

To optimize the discretized flux-limiter in Eq. (14), we define the mean squared error between N input-output pairs, $\{o_i(\{u_c^i\}), g_i\}$:

$$C = \frac{1}{2} \sum_{i=1}^N (o_i(\{u_c^i\}) - g_i)^2 \quad (16)$$

as the cost. Here, g_i is the high-resolution fluid velocity at the i -th grid position at time t_{n+1} and o_i is the shock-capturing method's prediction of the fluid velocity at time t_{n+1} from data at the previous timestep. o_i is a functional of a subset of data points $\{u_c^i\} = \{u_c^{i1}, u_c^{i2}, u_c^{i3}, \dots, u_c^{iN_c}\}$ indicated relative to the i -th grid position at time step t_n . Here, we used $N_c = 6$ data points at time t_n (see details in Appendix B) to predict a data point g_i at t_{n+1} , i.e. $\{u_c^i\} = \{u_{i-3}, u_{i-2}, u_{i-1}, u_i, u_{i+1}, u_{i+2}\}$. Thus, $o_i(\{u_c^i\})$ is the integration obtained with the flux-limiter method defined in Eqs. (4), (9), (10), (14) given a set of 6-points $\{u_c^i\}$:

$$o_i(\{u_c^i\}, t_{n+1}) = u_i(t_n) - \frac{\Delta t}{\Delta x} \Delta F(\{u_c^i\}, \{b_i\}, t_n). \quad (17)$$

Here, $\Delta F(\{u_c^i\}, \{b_i\}, t_n)$, defined via Eqs. (12) and (13), is the difference of the two fluxes defined in Eq. (4). The minimum of the cost function, Eq. (16), can be computed exactly by finding the unique root, \mathbf{b} , of the equation $\frac{\partial L}{\partial \mathbf{b}} = 0$, that is:

$$\sum_{i=1}^N \left(u_i - g_i - \frac{\Delta t}{\Delta x} \Delta F^i \right) \left(-\frac{\Delta t}{\Delta x} \right) \Delta s_i \Delta F_{2,3}^i = 0. \quad (18)$$

In Eq. (18), $\Delta F^i = \Delta F(\{u_c^i\}, \{b_i\}, t_n)$ is defined via Eqs. (12) and (13). $\Delta s_i = [\Delta r_i, \Delta r_{i-1}]$ is a $K \times 2$ matrix with Δr_i defined in Eq. (15). $\Delta F_{2,3}^i = [\Delta F_2^i, \Delta F_3^i]^T$ with components ΔF_2^i and ΔF_3^i defined via Eq. (13).

Solving Eq. (18) reduces to solving a linear equation $\mathbf{A} \cdot \mathbf{b} = \mathbf{C}$ that yields $\mathbf{b} = \mathbf{A}^{-1} \cdot \mathbf{C}$. Here, $\mathbf{A} = \Delta r_F \cdot (\Delta r_F)^T$ and $\mathbf{C} = \frac{\Delta t}{\Delta x} \sum_{i=1}^N O_G^i \Delta r_F^i$, where Δr_F is a $K \times N$ matrix with each column Δr_F^i a $K \times 1$ vector defined as $\Delta r_F^i = (\Delta s_i)(\Delta F_{2,3}^i)$.

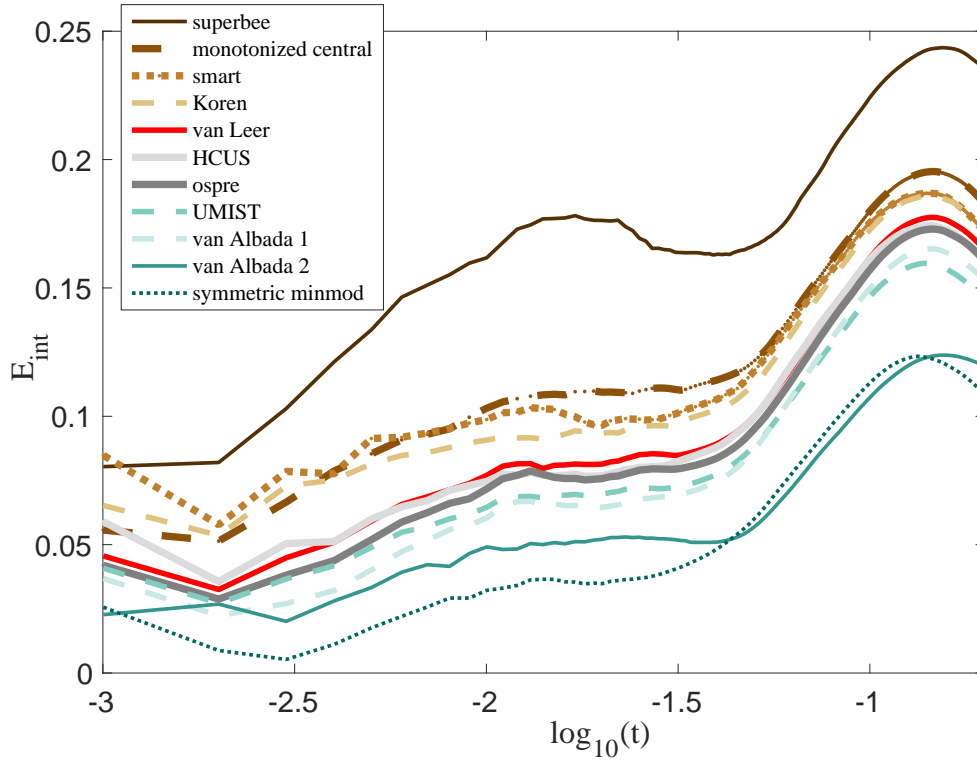


FIG. 2. Learning a $2\times$ coarse-grained flux limiter. We plot the error relative to our machine learned flux limiter (so, our flux limiter’s error relative to itself is zero, indicated by the x -axis) integrated across the spatial dimension, E_{int} , calculated for a set of standard flux limiters using $K = 20$ bins versus (log of) time. Here, a positive value for E_{int} indicates worse accuracy for the limiter being compared to. This means that, compared to all standard limiters, the $2\times$, $K = 20$ bin learned limiter performs better. Also, note that, similarly to what we saw in Fig. 1, the standard limiters are ordered with respect to their performance with some performing better and some worse relative to the machine learned limiter.

Finally, $O_G^i = u_i - g_i - \frac{\Delta t}{\Delta x} \Delta F_1^i$. Note that ΔF_1^i is defined via Eq. (13) and we recall that K is the size of the discretized flux limiter (i.e. the size of \mathbf{b}). Hence, each matrix \mathbf{A} (or \mathbf{C}) is a function of N training data points.

We wish our estimates of each segment of the flux limiter, $\phi_k(r)$, to have the same variance. Choosing this discretized space wisely is an important step. Our choice was to discretize the flux limiter such that each segment contained an equal number of training data points.

We used the above method with different coarse-grainings of the high-resolution dataset as training data in order to find optimal flux limiters, $\phi_k(r)$, for a set of coarse-grainings.

D. Hyperparameter Optimization of a Discretized Flux Limiter

The cost function defined in the previous section is intended to optimize a discretized flux-limiter for a given coarse-graining, CG , number of bins, K , and diffusion parameter, μ . We automated the generation of training and test data, the training of a discretized flux-limiter, and the testing of the learned limiter, to yield a function that produces the cost C as defined in Eq. (16) for a given CG , K , and μ . This ap-

proach leads to very good flux limiters for a particular set of parameters, however, the question remains as to whether we can find limiters that function well in a more general context. To attack this issue, we extended our approach by optimizing over (hyper)parameters. By averaging the cost for a learned flux-limiter over all segments,

$$\bar{C} = \sum_{k=1}^K C_k / K. \quad (19)$$

In particular, we used an optimizer to produce a flux-limiter that minimizes \bar{C} within the region defined by $\mu \in [0.005, 0.0248]$, $CG \in [2, 10]$, and $K \in [2, 38]$.

IV. RESULTS

We generated 500 Burgers’ simulations with 500 random initial conditions that have in total 160M data points. We attained good convergence of training results even with just 80 simulations (i.e. using less than 30M data points). For a discretization into 20 segments, the solution to \mathbf{b} was estimated with 1.5M data points per element and hence had a standard error of 0.0008. For this case, diagonalization was performed

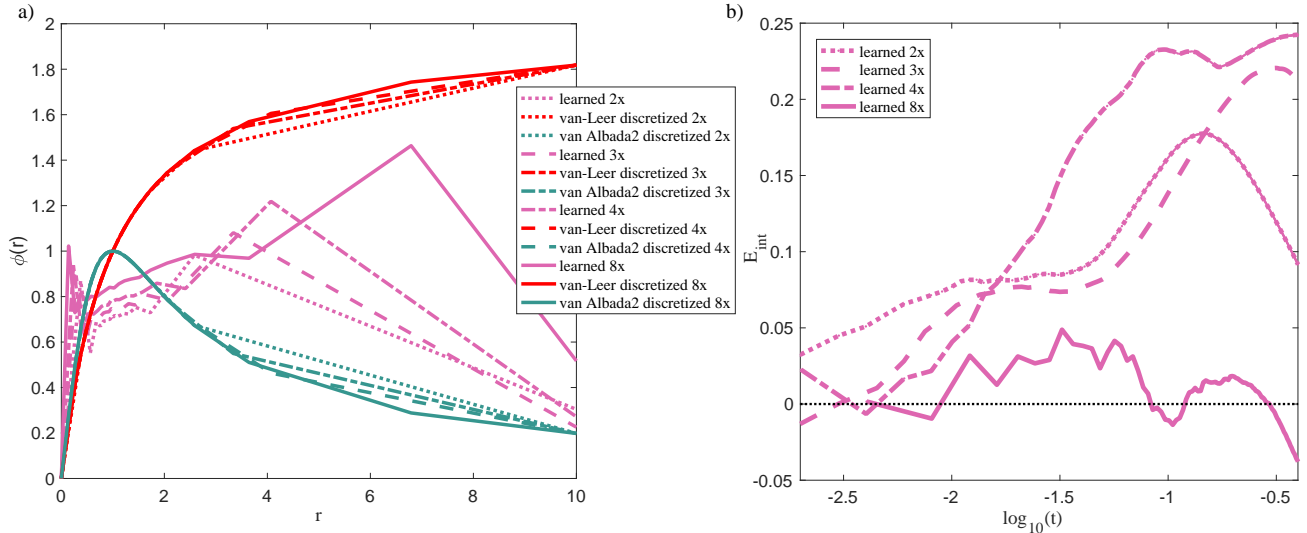


FIG. 3. (a): $K = 20$ bin machine learned limiter functions $\phi(r)$, van Leer, and van Albada 2 limiters plotted using the same discretized bins from 4 different coarse grained cases: $2\times$, $3\times$, $4\times$, and $8\times$. (b): Corresponding integrated relative errors, E_{int} (20), between the learned flux limiters with van Leer as a function of (log) time as compared to the ground truth for $2\times$, $3\times$, $4\times$, and $8\times$. Note that the machine learned limiters are not constrained to go through $(r, \phi) = (1, 1)$ (and, in this case, they do not).

on the inverse of the square matrix \mathbf{A} of size $K \times K$ with maximal K being $K = 20$ segments. Better standard errors were obtained with fewer segments, but at the cost of worse resolution of the limiter.

We validated our learning model on a subset of hold-out data which contained samples, $\{u_c^i\}$, from about 20 simulations.

We compared our optimized flux limiter with a set of standard flux limiters (sFLs). We computed the spatially integrated relative error

$$E_{\text{int}} \equiv \sum_i \left(\frac{e_i^{\text{sFL}} - e_i^{\text{learned}}}{e_i^{\text{learned}}} \right), \quad (20)$$

where the error at a given grid location, i , for each flux limiter is

$$e_i = o_i - g_i. \quad (21)$$

Note that this error, as defined, is positive when the learned limiter outperforms a given sFL. We investigated $K = 2, 5,$ and 20 segment flux limiters. Optimized flux limiters for all values of K were better than the discretized van Leer limiter (i.e. the relative error was everywhere > 0 with an average improvement of about 10%).

In Fig. 2, we plot the integrated relative error of our optimized flux limiter with $K = 20$ versus a set of eleven sFLs. Here, CG is $2\times$ and $r \in [0.0, 10.0]$. Note that the optimized limiter performs better than all other limiters investigated. Here, the symmetric minmod limiter performs best, but still reaches 10% greater error relative to the optimized limiter.

We plot optimized limiters, $\phi_k(r)$ in Fig. 3(a). Also, included in the plot are van Leer and van Albada 2 limiters for reference. These two limiters are commonly-used limiters and

bound the learned $K = 20$ limiters. For this analysis, equal-variance bins (see Sec. III C) were computed individually for coarse grainings of $2\times$, $3\times$, $4\times$, and $8\times$ (transitioning from dotted to solid magenta lines in Fig. 3(a)). Note that the smallest coarse grained case ($2\times$) has the smallest first slope b_1 in the first linear piece of $\phi(\{b_i\}, r)$, see Table I. As we in-

Coarse graining	$2\times$	$3\times$	$4\times$	$8\times$
First slope	2.33	3.11	4.02	7.28

TABLE I. First slope b_1 of the flux limiter obtained for 4 different coarse grainings shown as 4 solid lines in Fig. 3(a). Note that b_1 approximates the coarse-graining.

crease the coarse graining to a value larger than $2\times$, we see an increase in the slope of this first segment where b_1 roughly tracks the value of the coarse-graining.

In Fig. 3(b), we show errors, E_{int} , relative to the van Leer limiter, as a function of time, t . Note that for $2\times$ through $8\times$ coarse grainings, the optimized limiters perform best, but for $10\times$ (not plotted in (a)), the discretized van Leer limiter performs better. Note that here, we compare with the continuous van Leer limiter.

Upon inspection of Fig. 3, the general form of the learned limiters is 1) an initial (small r) sharply sloped kink that gets sharper as coarse-graining increases, 2) a subsequent roughly linear region with low-amplitude fluctuations, and 3) a final (large r) kink that is less sharply sloped than the initial kink. In Fig. 4, we visualize this pattern by plotting the bin widths (Fig. 4(a)) and integrated slopes (Fig. 4(b)), $\sum_{i=1}^K b_i$. The main patterns to point out here are that bin widths decrease for small r and increase for large r , while the integrated slopes are virtually identical as a function of coarse-graining, with the exception that they scale roughly with the coarse-graining.

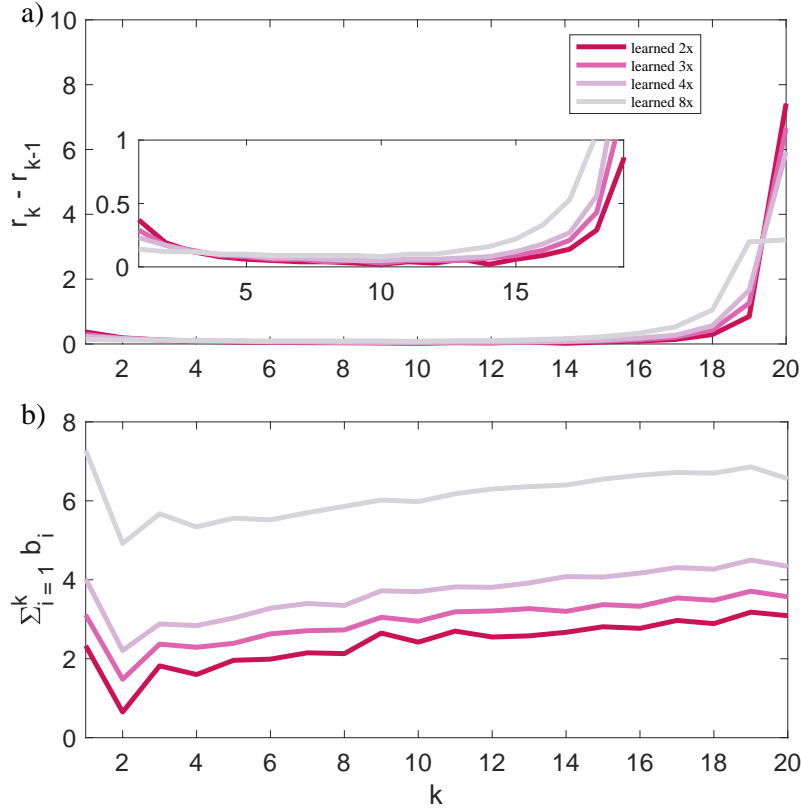


FIG. 4. Patterns in the scaling of learned flux limiters. a) Bin widths vs. k . Note the inversion of bin widths from left to right. Larger coarse grainings have smaller bin widths close to $r = 0$ and vice-versa for large r . b) The cumulative sum of the slopes, $\sum_{i=1}^k b_i$. This function has the same form across coarse-grainings but scales as a function of coarse-graining. Note also that b_1 is proportional to the coarse-graining, and the bulk of the k points occur in the roughly linear region with low-amplitude fluctuations ($r \in [0.5, 2.0]$) in Fig. 3(a).

Note also (in Tables II and III) that $r_k \sim 1.0$ when $k \sim K/2$, $r_K \sim CG$, and $b_1 \sim CG$.

Fig. 5 demonstrates the outcome of a flux limiter optimization in the hyperparameter subspace, $\{CG, K, \mu\}$, defined in Sec. III D. For this optimization, we selected the Differential Evolution²⁴ optimizer from *mystic*^{25,26} with the coarse-graining and number of bins restricted to be integers. A population of twenty-two initial points (CG, K, μ) , chosen at random from within the set of valid solutions, was mutated at each iteration. Thus, each new generation contained twenty-two candidate solutions per iteration. The optimizer continued to generate new candidate solutions until the change in candidate solutions was less than 10^{-10} over 100 iterations. We used 50 simulations to build each training set, and 10 simulations for each test set, where each simulation was run for $t = 800$ steps. New training (and test) data is generated for each new combination of (CG, K, μ) as part of the automated procedure.

In Fig. 5(a), we plot the learned flux limiters at select iterations as the hyperparameters converge. Note that as the learned limiters improve (with regard to the cost, in Fig. 5(c)), there is a convergence onto a positive linear slope at large r , and a convergence of the mid-segment $r_{K/2}$ of the limiter to roughly $(r, \phi) = (1, 0.6)$. In comparing Fig. 5(b) and

Fig. 5(c), it is apparent that the convergence of the cost is primarily driven by the convergence of the coarse-graining, CG , and secondarily the diffusion parameter, μ , while the number of bins, K , has little effect (also see Table IV). The lack of dependence of the cost on K makes sense, given that for all learned discretized flux limiters, the bulk of the line segments, r_i , occur in the roughly linear region, $r \in [0.5, 2.0]$, where the slope b_i exhibits only low-amplitude fluctuations. Essentially, as long as K is large enough to produce the initial and final kinked segments, any remaining extraneous segments appear to condense in the roughly linear region around $r = 1$.

It also appears that later in the convergence of the cost, where CG is fixed and μ is still converging, that the value of μ may primarily impact the shape of the limiter through ϕ_K and the slope b_K for the last line segment. In early iterations, where CG and μ are not nearly converged, we can see that at the mid-segment $r_{K/2} = 1.0$, but $\phi_{K/2} \neq 0.6$. As CG and then μ converge, we find $(r, \phi) = (1, 0.6)$.

The flux limiter that is learned in the hyperparameter optimization is given in Tables V and VI, and roughly follows the ‘rules’ established for r and b in Tables II and III. Specifically, learned limiters have an initial kinked region with a large slope, a final kinked region with a smaller slope, and a smaller roughly linear region around $r_k \sim 1.0$ when $k \sim K/2$.

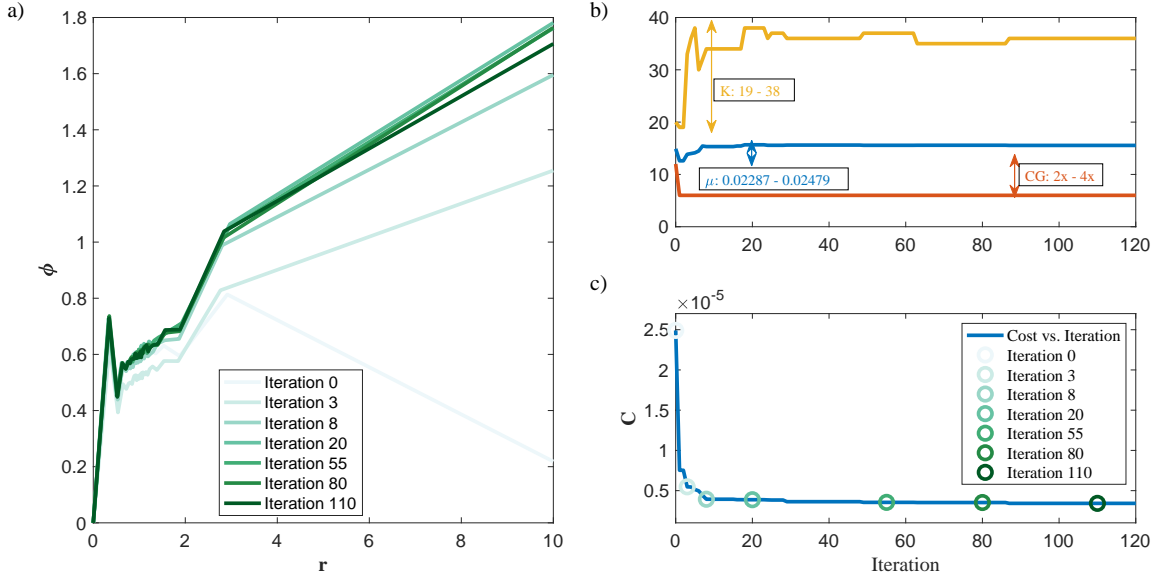


FIG. 5. Finding optimal flux limiters across multiple hyperparameters. a) A sequence of flux limiters learned over multiple iterations of optimization. The legend indicates the coarse-graining and the number of bins for which the flux limiter performs best, and the iteration at which it was found. b) Parameter convergence vs. iteration. Double headed arrows indicate the scale of parameter variation. Number of bins (yellow), coarse graining (red), diffusion parameter, μ (blue). c) The cost as a function of iteration. Circles denote iteration steps for flux limiters plotted in a). Note, in comparing b) and c), that convergence of the cost is primarily driven by CG , while K appears to have little effect.

Additionally, we see that generally $r_K \sim CG$ and $b_1 \sim CG$.

V. DISCUSSION

Here, we presented a framework for the data-driven determination of optimal flux limiters for the coarse-grained Burgers' equation. The framework consists of an internal optimizer computable with numerical linear algebraic methods, which can optionally be further optimized via a hyperparameter search over problem-specific parameters such as the number of bins in the limiter, the coarse-graining of the data, and the diffusion parameter (for Burgers' equation this is the only physical parameter in the problem).

Similar, data-driven approaches to the integration of partial differential equations have been undertaken²⁷. Here, by focusing on optimizing flux limiters, we attacked a central component of shock-capturing methods for integrating fluids. This allows our flux limiters to be essentially plug-and-play components for many existing numerical codes. We caution, however, that further work must still be done to understand how generally valuable our results are for fluid equations other than Burgers'. Information as to whether and how the regularities discovered in learned limiters change dependent on the target system may be useful for understanding the structure of shock-capturing codes more generally.

We chose to measure the quality of a discretized flux limiter by minimizing the mean-squared misfit for the limiter using 6 grid-point segments from the training data, averaged over all segments (as in Eq. (19)). We showed that under

this condition, when searching for a generally optimal limiter across a range of hyperparameters, flux limiters should be designed with the following rules-of-thumb: they should have 1) a fixed point at $(r, \phi) = (0, 0)$, 2) a first segment with a slope of $b_1 \sim CG$, 3) a second segment with a negative slope $b_2 < 0.0$, followed by 4) a roughly linear region around $r = 1$, $\phi \in [0.5, 1.0]$, and $k \sim K/2$, and 5) a larger final region where $r_K \sim CG$. It is interesting to note that the $(r, \phi) = (1, 1)$ constraint, which is due to a requirement of second-order accuracy of the shock capturing scheme and Lipschitz continuity of ϕ ²¹, is not obeyed, yet these limiters, nonetheless, perform better than standard limiters.

A main advantage of our limiters seems to be the flexibility allowed by the multiple segments that make up their shape. As opposed to the bent or bowed shapes of standard limiters, multiple segment limiters allow a spring-like compression that, at least for Burgers' equation, allows for an improvement in their performance.

In Fig. 6a, we show how our machine learned $8 \times$ -coarse-grained limiter fits with respect to the 2nd-order TVD region²¹. Full containment within the 2nd-order TVD region is a sufficient, but not necessary, condition to eliminate the possibility of Gibbs effects in 2nd-order shock capturing schemes (see discussion around Eqs. 2.15 and 2.16 in²¹). To confirm numerically that our limiters do not exhibit a Gibbs effect, we plot the evolution of a sinusoidal initial condition for $8 \times$ -coarse-grained initial data. Note that the van Albada 2 limiter is partially outside of the 2nd-order TVD region in Fig. 6a, and exhibits a distortion of the sinusoidal form in Fig. 6b (particularly, away from the shock). Conversely, al-

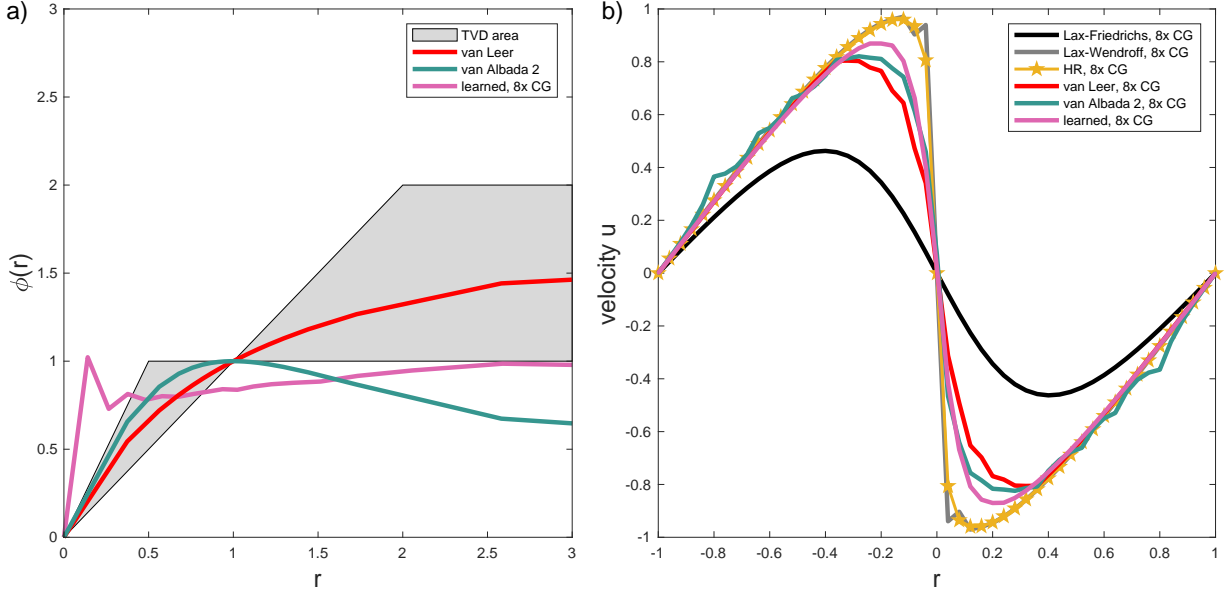


FIG. 6. Flux limiters and the 2nd-order TVD region. a) Plots of three flux limiters as they compare to the 2nd-order TVD region. Note that both the $8\times$ -coarse-grained limiter learned with our machine learning methods and the van Albada 2 limiter extend outside of the 2nd-order TVD region. b) The evolution of a sinusoidal initial condition with first-order only (Lax-Friedrichs), second-order only (Lax-Wendroff), high-resolution first-order method (HR), and the three flux limiters plotted in a). Note that the $8\times$ -coarse-grained limiter captures the shock more accurately than the others and, even though it does not lie in the 2nd-order TVD region, nonetheless exhibits no Gibbs effect (as does the Lax-Wendroff method shown in gray).

though our $8\times$ -coarse-grained limiter is also not fully contained within the 2nd-order TVD region, it does not exhibit any visible Gibbs effect in Fig. 6b and is entirely concave (resp. convex) on the left (resp. right) side of the shock. The $8\times$ -coarse-grained limiter best captures the shock, and we see similar results for $2\times$ -, $3\times$ -, and $4\times$ -coarse-grained machine learned limiters (not shown).

Given the rules-of-thumb that we have observed, our results for finding an optimal limiter over the range of $CG \in [2, 10]$, $K \in [2, 38]$, and $\mu \in [0.005, 0.0248]$, could most likely be improved by fixing the number of bins K , constraining the limiter to follow the rules noted above, and rerunning using a number of simulations N_s similar to that used when solving for a fixed (CG, K, μ) .

For fixed (CG, K, μ) calculations, we used $N_s = 500$ with 500 random initial conditions, yielding in total 160M data points. For variable (CG, K, μ) calculations, we used $N_s = 100$ with 100 random initial conditions, using less than 30M data points. We used a smaller N_s for the hyperparameter calculations to help reduce the computational cost of training the limiter, at the expense of some accuracy in the learned flux limiter. We performed our calculations on the Darwin cluster at Los Alamos National Laboratory on a 22 core cluster, where simulations were run in parallel, one simulation per core.

The first 12 iterations in the hyperparameter optimization completed in just less than 48 hours, with restarts (i.e. further optimization runs) performed over the next several days.

Fixing K , and using a larger number of parallel cores, should be able to decrease the time to obtain results. As the limiter segments that condense around $r = 1$ are found to be very short, it may be interesting to attempt to learn if there is a relationship between the minimum number of bins required, the resolution of the limiter, and the resulting standard error. Another interesting study may be to discover the impact on the observed set of rules when $N_c \neq 6$, and if it has any impact on the shape or minimum number of bins.

Another interesting observation is that while we used a diffusion parameter of $\nu = 0.01$ in our simulations, we found a learned diffusion parameter of $\mu = 0.02471$ in our hyperparameter optimization (see Table IV). The difference is roughly a factor of 2, which counter-balances the difference in coarse-graining between our simulations and the learned limiter. Similar changes in effective diffusion are seen in analytical approaches to coarse-graining^{1,2}. It may be prudent to determine if the diffusion parameter can always be determined similarly for other choices of CG.

Here, we chose to develop and test our machine learning approach to discovering improved flux limiters using 2nd order shock-capturing methods. State-of-the-art methods such as the piecewise-parabolic methods^{17,28} (PPM, 4th order) or (weighted) essentially non-oscillatory²⁹⁻³¹ (ENO, WENO, 8th order) methods may also benefit from our machine learning approach.

Further, as the generation of training data contains some randomness, an improvement would be to modify Eq. (16) to

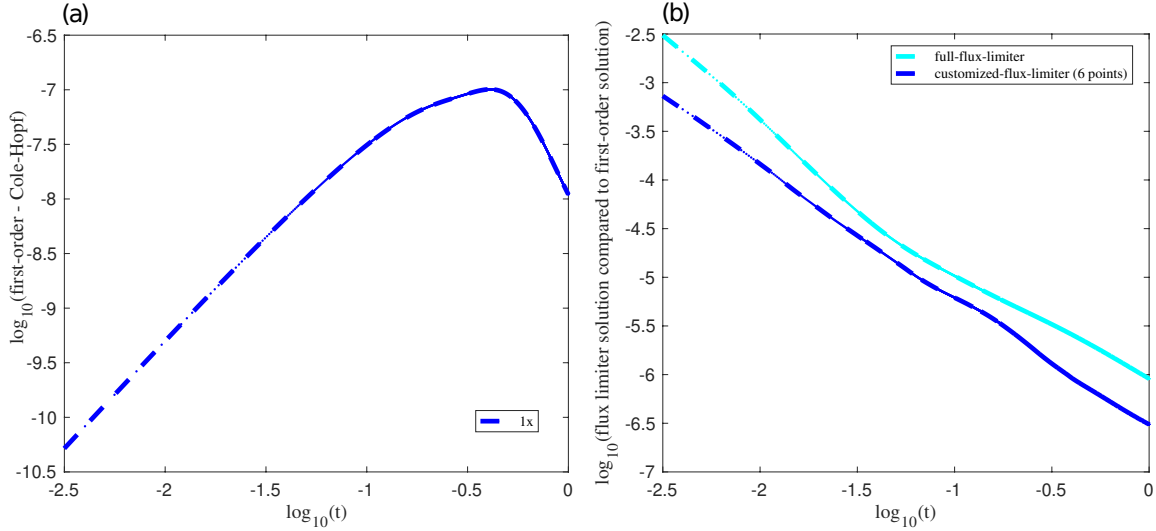


FIG. 7. a): Accuracy of the first-order, high-resolution solution as compared to the Cole-Hopf solution. See Sec. A. b): Relative error between the shock-captured solution computed with $\alpha = \max(|\frac{\partial F}{\partial u}|_u)$ and our customized Lax-Friedrichs flux with fixed $\alpha = 0.6$. See Sec. B

train flux limiters that minimize the expected mean squared error between input-output pairs:

$$C = \frac{1}{2} \sum_{i=1}^N \mathbb{E}(o_i(\{u_c^i\}) - g_i)^2. \quad (22)$$

In our study the impact of the randomness in the training data is mitigated by using a large number of simulations. Thus, we may be able to use significantly fewer simulations if we instead train the limiter on the expected mean-squared error. Additionally, our approach could be used to train flux limiters for *robustness* by minimizing \bar{C} , defined as:

$$\bar{C} = \sum_{k=1}^K \max C_k / K, \quad (23)$$

for a range of (CG, μ) , with C_k defined as in Eq. (22).

VI. CONCLUSIONS

We developed a theoretical framework that uses machine learning to train a continuous piecewise linear flux limiter by minimizing the mean-squared misfit to 6 grid-point segments of high-resolution data, averaged over all segments. We demonstrated our framework by producing a limiter that minimizes the misfit given a specific coarse graining, number of bins, and diffusion parameter. We then compared the learned limiter to a set of 11 common flux limiters, ranking the flux limiters by their log-error relative to high-resolution data. We

found that our $2\times$, $K = 20$ bin machine learned limiter produces less misfit everywhere, with respect to all 11 other limiters. Similarly, our $3\times$, $4\times$, and $8\times$ limiters, with $K = 20$ bins, generally outperformed all the other flux limiters. Our learned limiters all produced an initial kinked region with a large slope, a final kinked region with a smaller slope, and a smaller roughly linear region around $r_k \sim 1.0$ when $k \sim K/2$. Additionally, we see that generally $r_K \sim CG$ and $b_1 \sim CG$. A main advantage of our limiters seems to be the flexibility allowed by the multiple line segments, as opposed to the bent or bowed shapes of standard limiters, enabling a spring-like compression that, at least for Burgers' equation, yields an improvement in their performance. We also extended our framework to demonstrate we can machine learn piecewise-linear flux limiters that outperform standard limiters across a range of hyperparameter values of coarse-graining, number of discretized bins, and diffusion parameter. We found that learned limiters for the hyperparameter case also appear to generally adhere to the same rules as the piecewise linear limiters trained at fixed parameter values. Our study demonstrates a new approach to produce flux limiters that should be more broadly useful than standard limiters for general applications.

VII. ACKNOWLEDGEMENTS

We thank Robert Chiodi for discovering and correcting an error in our numerical code, which led us to correct a portion of our study. We thank Daniel Livescu for helpful discussions. Research presented in this article was supported

by the NNSA’s Advanced Simulation and Computing Beyond Moore’s Law Program at Los Alamos National Laboratory, and by the Uncertainty Quantification Foundation under the Statistical Learning program. Los Alamos National Laboratory is operated by Triad National Security, LLC, for the National Nuclear Security Administration of the U.S. Department of Energy (Contract No. 89233218CNA000001). The Uncertainty Quantification Foundation is a nonprofit dedicated to the advancement of predictive science through research, education, and the development and dissemination of advanced technologies. This document’s LANL designation is LA-UR-21-28444.

Appendix A: High-resolution solutions

In this Appendix, we discuss the solution obtained with a high-resolution, first-order scheme that we use to generate training and testing data, as compared to the discretized Cole-Hopf approach. We note again that the Cole-Hopf approach may exhibit instability when ν is small. The explicit form of the high-dimensional solution to Eq. (4) was obtained numerically as:

$$u_i(t_{n+1}) = u_i(t_n) + \Delta t(D\mathbf{v} + Gv^2) \quad (\text{A1})$$

with $D = \frac{1}{(4\Delta x)}[1, 0, -1]$, $\mathbf{v} = [u_{j-1}, u_j, u_{j+1}]^T$, and $G = \frac{\nu}{(\Delta x^2)}[1, -2, 1]$. Here v^2 indicates an element-by-element function giving the square of each element. Our high-resolution solution is very accurate when Δt and Δx stay small. This is confirmed in Fig. 7(a) where the high-resolution solutions are, at worst, within 10^{-6} of the discretized Cole-Hopf solution for coarse-grainings of $4\times$, and yet better for coarse-grainings of $2\times$ and below. Here, we use $\nu = 0.01$ and $\Delta t = 5 \times 10^{-4}$, $\Delta x = 5 \times 10^{-3}$ which are the values we used to generate our high-dimensional training dataset.

Appendix B: Customized Lax-Friedrichs flux

We explored methods to avoid computing the maximum over all u_i when calculating the value of the partial derivative w.r.t. u in Eq. (9). If possible, this would allow us to reduce the training input points in our machine learning method.

We found that replacing $\alpha = \max(|\frac{\partial F}{\partial u}|)_u$ with the constant $\alpha = 0.6$ gave us improved solutions relative to the full flux-limiter when compared to our high-resolution data.

In Fig. 7(b) we plot the relative error between the custom flux limiter and high resolution data compared to the relative error between the full maximum flux limiter and high resolution data for a high resolution simulation with $\Delta x = 2.5 \times 10^{-3}$, $\Delta t = 2.5 \times 10^{-4}$, $\nu = 0.005$. In the plot, we show the average solution error over twenty simulations with random initial conditions drawn from a uniform distribution from $\nu_{\min} = -1$ to $\nu_{\max} = 1$. Note that the modified method gives an error that is always less than the standard Lax-Friedrichs method. Therefore, we use this customized flux, f^{low} , with

$N_c = 6$ points, which appears in Eq. (17) in our machine learning model.

Appendix C: Learned flux limiters

Our discretized flux ratio bin edges, r_i , and machine learned coefficients, b_i , for flux limiters corresponding to $2\times$, $3\times$, $4\times$, $8\times$ of coarse graining (see Fig. 3(a)) are given in Tables II and III. Note that bin width $(r_i - r_{i-1})$ decreases for small r and increases for large r . Also note that $r_k \sim 1.0$ when $k \sim K/2$, $r_K \sim CG$, and $b_1 \sim CG$.

Similarly, solved r_i and b_i in the optimization of a discretized machine learned limiter in the region defined by $CG \in [2, 10]$, $K \in [2, 38]$, and $\mu \in [0.005, 0.0248]$ (see Fig. 5(a)) are given in Tables V and VI. The corresponding values of CG , K , and μ are given in Table IV.

Appendix D: Standard flux limiters

See Table VII for the flux limiters used for comparison in Figs. 1 and 2.

- ¹D. Besnard, F. H. Harlow, R. M. Rauenzahn, and C. Zemach, “Turbulence transport equations for variable-density turbulence and their relationship to two-field models,” Tech. Rep. (Los Alamos National Lab., NM (United States), 1992).
- ²J. D. Schwarzkopf, D. Livescu, R. A. Gore, R. M. Rauenzahn, and J. R. Ristorcelli, “Application of a second-moment closure model to mixing processes involving multicomponent miscible fluids,” *Journal of Turbulence*, N49 (2011).
- ³X. Zhou, C. Zhong, Z. Li, and F. Li, “Preconditioned jacobian-free newton–krylov fully implicit high order weno schemes and flux limiter methods for two-phase flow models,” *Nuclear Engineering and Technology* **54**, 49–60 (2022).
- ⁴N. Valle, X. Álvarez-Farré, A. Gorobets, J. Castro, A. Oliva, and F. X. Trias, “On the implementation of flux limiters in algebraic frameworks,” *Computer Physics Communications* **271**, 108230 (2022).
- ⁵R. Abedian, “A third-order weighted essentially non-oscillatory-flux limiter scheme for two-dimensional incompressible navier-stokes equations,” *Computational Methods for Differential Equations* (2022).
- ⁶R. Vinuesa and S. L. Brunton, “Enhancing computational fluid dynamics with machine learning,” *Nature Computational Science* **2**, 358–366 (2022).
- ⁷J. Tompson, K. Schlachter, P. Sprechmann, and K. Perlin, “Accelerating Eulerian fluid simulation with convolutional networks,” in *Proceedings of the 34th International Conference on Machine Learning-Volume 70* (JMLR. org, 2017) pp. 3424–3433.
- ⁸A. Mohan, D. Daniel, M. Chertkov, and D. Livescu, “Compressed convolutional lstm: An efficient deep learning framework to model high fidelity 3d turbulence,” arXiv preprint arXiv:1903.00033 (2019).
- ⁹B. Nadiga, C. Jiang, and D. Livescu, “Leveraging bayesian analysis to improve accuracy of approximate models,” *Journal of Computational Physics* **394**, 280–297 (2019).
- ¹⁰H. Chan, M. J. Cherukara, B. Narayanan, T. D. Loeffler, C. Benmore, S. K. Gray, and S. K. Sankaranarayanan, “Machine learning coarse grained models for water,” *Nature communications* **10**, 1–14 (2019).
- ¹¹J. M. Burgers, “A mathematical model illustrating the theory of turbulence,” in *Advances in applied mechanics*, Vol. 1 (Elsevier, 1948) pp. 171–199.
- ¹²H. Eberhard, “The partial differential equation $u_t + uux = \mu u_{xx}$,” (1942).
- ¹³J. D. Cole, “On a quasi-linear parabolic equation occurring in aerodynamics,” *Quarterly of applied mathematics* **9**, 225–236 (1951).
- ¹⁴H. Wilbraham, “On a certain periodic function,” *The Cambridge and Dublin Mathematical Journal* **3**, 198–201 (1848).
- ¹⁵S. Godunov, “A difference scheme for numerical computation of discontinuous solutions of fluid dynamics,” *Mat. Sb* **47**, 271–306 (1959).

	r_1	r_2	r_3	r_4	r_5	r_6	r_7	r_8	r_9	r_{10}	r_{11}	r_{12}	r_{13}	r_{14}	r_{15}	r_{16}	r_{17}	r_{18}	r_{19}	r_{20}	r_{21}
2x	0	0.37	0.56	0.68	0.76	0.82	0.87	0.91	0.95	0.98	1.00	1.04	1.07	1.13	1.15	1.21	1.3	1.44	1.73	2.58	10
3x	0	0.29	0.46	0.59	0.68	0.76	0.82	0.88	0.92	0.97	1.00	1.05	1.10	1.15	1.22	1.31	1.44	1.65	2.08	3.34	10
4x	0	0.23	0.40	0.52	0.62	0.71	0.78	0.85	0.91	0.96	1.01	1.07	1.13	1.2	1.28	1.4	1.58	1.85	2.41	4.07	10
8x	0	0.14	0.26	0.38	0.48	0.58	0.67	0.76	0.85	0.94	1.02	1.12	1.22	1.35	1.51	1.73	2.06	2.59	3.64	6.79	10

TABLE II. Discretized space r for $2\times$, $3\times$, $4\times$, and $8\times$ of coarse graining.

	b_1	b_2	b_3	b_4	b_5	b_6	b_7	b_8	b_9	b_{10}	b_{11}	b_{12}	b_{13}	b_{14}	b_{15}	b_{16}	b_{17}	b_{18}	b_{19}	b_{20}
2x	2.33	-1.68	1.17	-0.22	0.36	0.03	0.16	-0.02	0.52	-0.23	0.28	-0.15	0.03	0.09	0.14	-0.04	0.20	-0.08	0.29	-0.09
3x	3.11	-1.63	0.89	-0.08	0.10	0.24	0.08	0.02	0.32	-0.10	0.24	0.02	0.06	-0.07	0.17	-0.04	0.21	-0.06	0.23	-0.14
4x	4.02	-1.81	0.67	-0.04	0.19	0.25	0.12	-0.05	0.37	-0.02	0.12	-0.01	0.11	0.16	-0.01	0.10	0.14	-0.04	0.23	-0.16
8x	7.28	-2.36	0.75	-0.33	0.22	-0.04	0.18	0.16	0.16	-0.04	0.20	0.12	0.06	0.04	0.15	0.10	0.07	-0.02	0.16	-0.30

TABLE III. Line segment slopes b obtained for $K=20$ with $2\times$, $3\times$, $4\times$, and $8\times$ of coarse graining.

	CG	K	μ	\bar{C}
0	4x	20	0.02431	0.00002491
3	2x	33	0.02366	0.00000547
8	2x	34	0.02476	0.00000393
20	2x	38	0.02479	0.00000387
55	2x	37	0.02473	0.00000354
80	2x	35	0.02474	0.00000352
110	2x	36	0.02471	0.00000341

TABLE IV. Coarse graining, CG , number of bins, K , diffusion parameter, μ , and associated cost, \bar{C} , at selected iterations in the optimization of a discretized machine learned limiter in the region defined by $CG \in [2, 10]$, $K \in [2, 38]$, and $\mu \in [0.005, 0.0248]$.

- ¹⁶B. Van Leer, "Towards the ultimate conservative difference scheme. v. a second-order sequel to godunov's method," *Journal of computational Physics* **32**, 101–136 (1979).
- ¹⁷P. Colella and P. R. Woodward, "The piecewise parabolic method (ppm) for gas-dynamical simulations," *Journal of computational physics* **54**, 174–201 (1984).
- ¹⁸A. Harten, "High resolution schemes for hyperbolic conservation laws," *Journal of computational physics* **135**, 260–278 (1997).
- ¹⁹C.-W. Shu and S. Osher, "Efficient implementation of essentially non-oscillatory shock capturing schemes, 2," (1988).
- ²⁰D. Zhang, C. Jiang, D. Liang, and L. Cheng, "A review on tvd schemes and a refined flux-limiter for steady-state calculations," *Journal of Computational Physics* **302**, 114–154 (2015).
- ²¹P. K. Sweby, "High resolution schemes using flux limiters for hyperbolic conservation laws," *SIAM journal on numerical analysis* **21**, 995–1011 (1984).
- ²²M. Maritz and S. Schoombie, "Exact analysis of nonlinear instability in a discrete burgers' equation," *Journal of Computational Physics* **97**, 73–90 (1991).
- ²³B. Van Leer, "Towards the ultimate conservative difference scheme. ii. monotonicity and conservation combined in a second-order scheme," *Journal of computational physics* **14**, 361–370 (1974).
- ²⁴R. M. Storn and K. V. Price, "Differential evolution — a simple and efficient heuristic for global optimization over continuous spaces," *J. Global Optim.* **11**, 341–359 (1997).
- ²⁵M. McKerns, P. Hung, and M. Aivazis, "mystic: highly-constrained non-convex optimization and uq," (2009-), <https://uqfoundation.github.io/project/mystic>.
- ²⁶M. McKerns, L. Strand, T. J. Sullivan, A. Fang, and M. Aivazis, "Building a framework for predictive science," in *Proceedings of the 10th Python in Science Conference, 2011* (2011) pp. 67–78, <http://arxiv.org/pdf/1202.1056>.
- ²⁷Y. Bar-Sinai, S. Hoyer, J. Hickey, and M. P. Brenner, "Learning data-driven discretizations for partial differential equations," *Proceedings of the National Academy of Sciences* **116**, 15344–15349 (2019).
- ²⁸B. Tripathi, D. Espindola, and G. Pinton, "Piecewise parabolic method for simulating one-dimensional shear shock wave propagation in tissue-mimicking phantoms," *Shock Waves* **27**, 879–888 (2017).
- ²⁹A. Harten and S. Osher, "Uniformly high-order accurate nonoscillatory schemes. i," in *Upwind and High-Resolution Schemes* (Springer, 1997) pp. 187–217.
- ³⁰X.-D. Liu, S. Osher, and T. Chan, "Weighted essentially non-oscillatory schemes," *Journal of computational physics* **115**, 200–212 (1994).
- ³¹Y. Ha, C. H. Kim, Y. J. Lee, and J. Yoon, "Mapped weno schemes based on a new smoothness indicator for hamilton-jacobi equations," *Journal of Mathematical Analysis and Applications* **394**, 670–682 (2012).
- ³²P. L. Roe, "Characteristic-based schemes for the euler equations," *Annual review of fluid mechanics* **18**, 337–365 (1986).
- ³³B. Van Leer, "Towards the ultimate conservative difference scheme iii. upstream-centered finite-difference schemes for ideal compressible flow," *Journal of Computational Physics* **23**, 263–275 (1977).
- ³⁴P. Gaskell and A. Lau, "Curvature-compensated convective transport: Smart, a new boundedness-preserving transport algorithm," *International Journal for numerical methods in fluids* **8**, 617–641 (1988).
- ³⁵B. Koren, *A robust upwind discretization method for advection, diffusion and source terms* (Centrum voor Wiskunde en Informatica Amsterdam, 1993).
- ³⁶N. Waterson and H. Deconinck, "A unified approach to the design and application of bounded higher-order convection schemes," *Numerical methods in laminar and turbulent flow* **9**, 203–214 (1995).
- ³⁷F.-S. Lien and M. Leschziner, "Upstream monotonic interpolation for scalar transport with application to complex turbulent flows," *International Journal for Numerical Methods in Fluids* **19**, 527–548 (1994).
- ³⁸G. D. Van Albada, B. Van Leer, and W. Roberts, "A comparative study of computational methods in cosmic gas dynamics," in *Upwind and high-resolution schemes* (Springer, 1997) pp. 95–103.
- ³⁹M. Kermami, A. Gerber, and J. Stockie, "Thermodynamically based moisture prediction using roe's scheme," in *4th Conference of Iranian Aerospace Society, Amir Kabir University of Technology, Tehran, Iran*, Vol. 3 (Cite-seer, 2003).

	r_1	r_2	r_3	r_4	r_5	r_6	r_7	r_8	r_9	r_{10}	r_{11}	r_{12}	r_{13}	r_{14}	r_{15}	r_{16}	r_{17}	r_{18}	r_{19}	r_{20}	r_{21}	r_{22}	
110	0.0	0.35	0.52	0.63	0.71	0.76	0.80	0.83	0.86	0.88	0.90	0.91	0.93	0.94	0.96	0.97	0.98	0.99	1.00	1.01	1.02	1.03	
	1.04	1.06	1.07	1.09	1.11	1.13	1.16	1.19	1.24	1.30	1.40	1.56	1.88	2.84	10.00								

TABLE V. Solved discretized bin edge locations, r_i , in the optimization of a discretized machine learned limiter in the region defined by $CG \in [2, 10]$, $K \in [2, 38]$, and $\mu \in [0.005, 0.0248]$. The corresponding values of CG , K , and μ are found in Table IV.

	b_1	b_2	b_3	b_4	b_5	b_6	b_7	b_8	b_9	b_{10}	b_{11}	b_{12}	b_{13}	b_{14}	b_{15}	b_{16}	b_{17}	b_{18}	b_{19}	b_{20}	b_{21}	
110	2.11	-1.58	1.10	-0.27	0.49	-0.16	0.51	-0.05	0.09	0.37	0.75	-1.11	0.36	-0.37	0.98	-0.33	0.04	0.75	-1.37	1.27	0.77	
	-1.88	1.45	-0.28	0.93	0.25	0.07	0.29	-0.67	0.32	0.14	0.03	0.31	0.004	0.36	0.09							

TABLE VI. Solved line segment slopes, b_i , in the optimization of a discretized machine learned limiter in the region defined by $CG \in [2, 10]$, $K \in [2, 38]$, and $\mu \in [0.005, 0.0248]$. The corresponding values of CG , K , and μ are found in Table IV.

superbee³²: $\phi_{sb}(r) = \max(0, \min(2r, 1), \min(r, 2))$
monotonized central³³: $\phi_{mc}(r) = \max(0, \min(2r, 0.5(1+r), 2))$
smart³⁴: $\phi_{sm}(r) = \max(0, \min(2r, (1/4 + 3r/4), 4))$
Koren³⁵: $\phi_{kn}(r) = \max(0, \min(2r, \min((1/3 + 2r/3), 2)))$
van Leer²³: $\phi_{vL}(r) = \frac{r+|r|}{1+|r|}$
HCUS³⁶: $\phi_{hc}(r) = \frac{1.5(r+|r|)}{r+2}$
ospre³⁶: $\phi_{os}(r) = \frac{1.5(r^2+r)}{r^2+r+1}$
UMIST³⁷: $\phi_{um}(r) = \max(0, \min(2r, 1/4 + 3r/4, 3/4 + r/4, 2))$
van Albada 1³⁸: $\phi_{va1}(r) = \frac{r^2+r}{r^2+1}$
van Albada 2³⁹: $\phi_{va2}(r) = \frac{2r}{r^2+1}$
symmetric minmod³²: $\phi_{mm}(r) = \max(0, \min(1, r))$

TABLE VII. Mathematical expressions for the standard flux limiters used for comparison in Figs. 1 and 2